Microstructural evolution of UO2 pellets containing metallic particles of Ru, Rh and Pd during dissolution in nitric acid solution: 3D-ESEM monitoring

T. Cordara, Stephanie Szenknect, Renaud Podor, V. Trillaud, Laurent Claparede, X. F Le Goff, Adel Mesbah, C. Lavalette, N. Dacheux

Microstructural evolution of UO2 pellets containing metallic particles of Ru, Rh and Pd during dissolution in nitric acid solution: 3D-ESEM monitoring

T. Cordara, S. Szenknect, R. Podor, V. Trillaud, L. Claparede, X. Le Goff, A. Mesbah, C. Lavalette, N. Dacheux

PII: S0304-386X(19)30277-4
DOI: https://doi.org/10.1016/j.hydromet.2019.07.001
Reference: HYDROM 5098

To appear in: *Hydrometallurgy*

Received date: 27 March 2019
Revised date: 27 June 2019
Accepted date: 1 July 2019

Please cite this article as: T. Cordara, S. Szenknect, R. Podor, et al., Microstructural evolution of UO2 pellets containing metallic particles of Ru, Rh and Pd during dissolution in nitric acid solution: 3D-ESEM monitoring, Hydrometallurgy, https://doi.org/10.1016/j.hydromet.2019.07.001

Microstructural evolution of UO_2 pellets containing metallic particles of Ru, Rh and Pd during dissolution in nitric acid solution: 3D-ESEM monitoring

T. Cordara[a], S. Szenknect[a,*], R. Podor[a], V. Trillaud[a], L. Claparede[a], X. Le Goff[a], A. Mesbah[a], C. Lavalette[b], N. Dacheux[a].

[a] ICSM, CEA, CNRS, ENSCM, Univ Montpellier, site de Marcoule, 30207 Bagnols sur Cèze, France.

[b] ORANO NC, 1 pl. Jean Millier, 92084 Paris La Défense, France.

*Corresponding author: stephanie.szenknect@cea.fr

Abstract

Uranium dioxide containing 3 mol.% platinum group metals (PGMs) (Ru, Rh, Pd) was synthesized by hydroxide precipitation. The powders were converted to oxides, pelletized and sintered to prepare dense pellets of UO_2 incorporating PGMs particles. The characterization techniques performed revealed a microstructure similar to that of spent nuclear fuel (SNF). Dissolution tests in nitric acid demonstrated that in the presence of PGMs, the uranium dissolution rate was increased and the induction period was shortened. We used a new method based on the acquisition of Environmental Scanning Electron Microscopy (ESEM) micrographs recorded at three tilt angles and at different dissolution times. This method allowed the reconstruction of the topography of the solid/liquid interface. By monitoring the evolution of the solid/liquid interface during dissolution by means of 3D reconstructions, we were able to observe preferential dissolution zones in the vicinity of the PGMs particles and to determine microscopic dissolution rates for several regions of interest. PGMs particles were found mainly at the grain boundaries. In 0.1 M HNO_3 solution at 60°C, the normalized dissolution rate for uranium at the grain boundaries reached $R_L(U) = (7 \pm 1)\times10^{-2}$ $g.m^{-2}.d^{-1}$, a value similar to the normalized dissolution rate determined for the whole image over the first 30 days of the experiment. This result showed that the dissolution occurred mainly at the UO_2 grain boundaries in the vicinity of PGMs particles. Furthermore, the 3D reconstructions of the solid/liquid interface were used to determine the evolution of the surface area of the pellet. By combining the weight losses determined at the macroscopic scale using the uranium concentrations in solution with the reactive surface area values, it was possible to estimate an effective normalized dissolution rate for the whole pellet.

1. Introduction

Spent nuclear fuel (SNF) is a complex, heterogeneous system in terms of its chemical composition and microstructure[1-4]. The irradiated oxide fuel forms a complex multiphasic system

containing more than 30 fission products[5-6]. The final composition of the spent fuel depends on the initial fuel composition, the initial enrichment in ^{235}U, the type of reactor and the burn-up. These fission products are generally classified in representative groups presenting similar physicochemical behavior. The noble metals group, which is represented in SNF mainly by Mo, Ru, Rh, Pd and Tc, is not incorporated in the crystal lattice of UO_2, but found as metallic inclusions trapped in the inter- and intra-granular pores and in the grain boundaries[7-9]. In light water reactor UO_2 fuel, the metallic precipitates are spherical particles ranging in size from 10 nm to 300 nm, potentially aggregated in larger particles (of several microns). The size of the metallic particles depends on the burn-up and on their position in the UO_2 pellet. The zones that experienced the highest temperatures in the fuel contain the largest metallic particles, measuring up to several µm in diameter[8, 10]. These metallic particles are alloys whose composition varies depending on the burn-up, the initial composition of the fuel, the oxygen/metal ratio and the thermal conditions in the fuel rods. They are found primarily in the hexagonal close-packed (hcp) ε-Ru (Mo, Tc, Rh Pd) phase[8, 11]. The mechanisms of their formation at the atomistic scale and migration within the grains at the microscopic scale remain partly unknown, despite recent insights provided through the irradiation and annealing of ceria thin films doped with Mo, Ru, Rh, Pd and Re (used as a surrogate of Tc)[12].

It is useful to characterize ε-particles because of their potential role in the behavior of the spent fuel during the initial storage, during the storage in geological repositories[13], and during the first step of the SNF recycling process[14-15]. After their residence time in the reactor, SNF from a pressurized water reactor (PWR) is dissolved in a hot, concentrated (> 4 $mol.L^{-1}$) solution of nitric acid. The resulting solution is suitable for the reprocessing of U and Pu with the PUREX process. During this step, however, insoluble residues accumulate in the dissolver, potentially leading to crud formation or plugging of pipes or to loss of Pu[14, 16]. The insoluble residues are mainly metallic particles and oxide precipitates rich in Mo, Tc, Ru, Rh, Pd, and Zr that also incorporate substantial amounts of Pu[14, 16-19]. The composition of the insoluble residues depends mainly on the dissolution conditions, especially nitric acid concentration, but also on the time elapsed between the end of dissolution and the clarification of the dissolver solution[16]. The amount of insoluble residues increases with the fission yield and therefore depends on the initial fuel composition and the burn-up[14, 20]. Adachi et al.[14] indicated that the relative ratio of noble metals in the insoluble residue was different from that determined in the spent PWR fuels burnt between 7000 and 39000 $MWd.t^{-1}$. Currently, Pu-rich MO_x fuel is the subject of a new challenge: the aim is to develop alternative methods for the dissolution of high burn-up MO_x fuels that limit the amount of insoluble residues[15, 21-22].

Besides these issues, the presence of noble metal particles in the fuel can affect the dissolution rate of the UO_2 matrix during the first step of the recycling process. The dissolution mechanism of UO_2 in nitric acid solutions involves the oxidation of uranium (IV) to uranium (VI) at the solid/solution interface. According to the literature, the most likely mechanism is initiated by redox

reaction between UO_2 and NO_3^- at the solid/solution interface[23]. This reaction is considered to be slow, but it produces NO_2, which leads to the formation of nitrous acid in solution. This period associated with slow dissolution kinetics has been observed by various authors[24-26]. Cordara et al.[27] performed dissolution experiments in less concentrated nitric acid solutions (0.1 to 4 $mol.L^{-1}$) and observed that the duration of the induction period was variable depending on temperature and nitric acid concentration, but ended systematically after a UO_2 weight loss of 0.5%, indicating that the required concentration of catalytic species might be reached at this stage. Nitrous acid is suspected to be the species increasing the dissolution rate of UO_2[28-32].

Ikeda et al.[33] observed a higher dissolution rate for pulverized irradiated fuels than for UO_2 in 3 to 4 $mol.L^{-1}$ HNO_3 at room temperature; apart from the difference in their densities and effective surface areas, they attributed this acceleration to the presence of certain fission products. They showed that the induction period was shortened for powdered irradiated fuels and that the HNO_2 concentration remained constant. They proposed that oxidants other than HNO_2 and NO_3^- species participated in the dissolution mechanism of irradiated fuels. According to standard reduction potentials[34] ($E°$ (Ru^{2+}/Ru) = 0.455 V/NHE; $E°$ (Rh^{+}/Rh) = 0.600 V/NHE; $E°$ (Rh^{3+}/Rh) = 0.758 V/NHE; $E°$ (Pd^{2+}/Pd) = 0.951 V/NHE), platinum group metals (PGMs) cannot directly oxidize tetravalent uranium to UO_2^{2+} ($E°$ = 0.327 V/NHE for UO_2^{2+}/U^{4+}). However, all of these redox couples (except Pd^{2+}/Pd), as well as Ru^{3+}/Ru^{2+} ($E°$ = 0.2487 V/NHE), are able to reduce nitrate ions to HNO_2 in nitric acid solutions ($E°$ (NO_3^-/HNO_2) = 0.934 V/NHE). In addition, Kim et al.[35] reported redox reactions showing not only that Ru(IV) can oxidize UO_2, but also that Ru(III) reduces NO_3^- to HNO_2 and is oxidized to Ru(IV). Thus, if the dissolution of Ru metal occurs in nitric acid solution and leads to the formation of Ru(III) species, the redox reaction with NO_3^- may produce two oxidants for UO_2: HNO_2 and Ru(IV). All of these redox reactions involve the dissolution of PGMs particles. Although the dissolution rate of noble metal particles was low, Matsui et al.[36] were able to measure it for Mo-Ru-Rh-Pd micrometric particles in 3 $mol.L^{-1}$ boiling HNO_3 solution. Also, Ikeuchi et al.[15] showed that the 8-11 $mol.L^{-1}$ boiling HNO_3 solutions used to dissolve fragments of MO_x fuel irradiated in a fast breeder reactor contained ^{106}Ru. Thus, the acceleration effect of the noble metal particles could be partially explained by the dissolution of the PGMs (Rh, Pd and Ru) producing a sufficient concentration of HNO_2 in solution to strongly reduce the duration of the induction period.

Ikeda et al.[37] previously highlighted the acceleration effect of PGMs particles (Rh, Pd and Ru) incorporated in UO_2 powder on the dissolution of UO_2 in nitric acid solutions using synthesized model compounds. They showed that among these noble metals, Rh had the strongest acceleration effect. This effect was considered to be catalytic, as it was found to be independent of the mole fraction of Rh incorporated in UO_2. Finally, they suggested that direct interactions between UO_2 and PGMs particles were required to increase the dissolution rate. To draw this conclusion, Ikeda et al.[37] introduced a piece of Pd metal into the nitric acid solution and did not observe any acceleration. It is noteworthy that

considering the redox potentials of the Pd^{2+}/Pd and NO_3^-/HNO_2 couples, Pd metal should not be able to reduce nitrate ions in nitrous acid. Thus, the experiments performed by Ikeda et al.[37] offered key information, but were not sufficient to conclude that direct contact between UO_2 and noble metal particles was required.

In order to obtain insights about the acceleration effect of the PGMs particles on the dissolution of UO_2 in nitric acid solutions, UO_2 pellets incorporating (or not incorporating) 3 mol.% PGMs (Ru, Rh and Pd) were used as model compounds. The impact of the presence of PGMs particles on the rate of dissolution of UO_2 was first evidenced using macroscopic dissolution tests performed in 0.1 $mol.L^{-1}$ HNO_3 solution at 60°C. The evolution of the solid/solution interface during the dissolution of the model compounds was also investigated at the microscopic scale in order to evidence preferential dissolution zones in the vicinity of PGMs particles. This work was carried out using a new method developed by Podor et al.[38]. This method is based on the acquisition of Environmental Scanning Electron Microscopy (ESEM) micrographs of a selected region at the surface of the material at different dissolution times. ESEM monitoring allowed determining an accurate dissolution rate at the local scale and eliminated issues associated with the quantification of the effective surface area of the sample at the macroscopic scale. This method made it possible to know if direct contact between UO_2 and PGMs particles modified the kinetics of dissolution.

2. Experimental

1. Preparation of UO_2 + PGM pellets

Uranium dioxide was doped with PGMs by hydroxide precipitation according to a protocol initially developed by Martinez et al.[39] This route consisted in mixing 3.5 mL of uranium (IV) chloride stock solution (0.7 $mol.L^{-1}$ in 6 $mol.L^{-1}$ HCl) with 0.5 mL of a solution of PGM chloride, prepared by dissolving the PGM salts (hydrated ruthenium (III) chloride (Sigma Aldrich, 99,9 %), hydrated rhodium (III) chloride (Sigma Aldrich, 99,9 %) and palladium (II) chloride (Sigma Aldrich, 99,9 %)) in 1 $mol.L^{-1}$ HCl solution (Sigma Aldrich). The calculated stoichiometry of the cations in solution was: Rh:U = 0.003 mol.%; Pd:U = 0.0108 mol.%; and Ru:U = 0.0162 mol.%, leading to Σ_{PGMs}:U = 0.03 mol.%. The mixture of cations was then poured into a large excess of ammonium hydroxide (400%) at room temperature. Precipitation was found to be instantaneous. The precipitate was further aged in solution for 30 minutes under magnetic stirring. The precipitated powder was then separated from the supernatant by centrifugation at 4500 rpm. The resulting powder was finally washed several times with deionized water, then once with ethanol, in order to eliminate the remaining ammonium hydroxide. After this washing step, the sample was introduced into a flask with 50 mL of ethanol. This suspension was then placed under vacuum and stirred mechanically at 40°C. After the complete evaporation of the solvent, the stirring was maintained for a few minutes, and then the flask was filled

with nitrogen. The powdered precursor was finally converted to its oxide form by a single calcination step performed at 800°C for 4 hours under reducing atmosphere (Ar + 5% H_2).

Dense pellets of uranium dioxide doped with PGMs were prepared by sintering. First of all, the oxide powder was ball-milled for 30 minutes at a frequency of 30 Hz in zirconia jars using a Retzsch mixer mill (MM 400). Next, a tri-shell die of 5 mm in diameter was used to uniaxially press the powder at 500 MPa, producing green pellets of 1 to 2 mm in thickness with a densification rate of about 50%. The green pellets were sintered for 8 hours at 1500°C under reducing atmosphere (Ar + 5% H_2). The resulting dense pellets of 150 to 200 mg in mass were then fully characterized.

2. Characterization of samples

The stoichiometric composition of each sample was determined by complete dissolution of a weighted amount of oxide powder in 10 mL of 2 mol.L^{-1} nitric acid solution at 60°C, followed by analysis of the elemental concentrations in the obtained solution diluted in 0.2 mol.L^{-1} HNO_3 by inductively-coupled plasma atomic emission spectroscopy (ICP-AES, Spectro Arcos). The supernatants collected during the washing steps of the synthesis protocol were also analyzed by ICP-AES to determine the precipitation yield. The intensity of the emitted signal was recorded at two wavelengths characteristic of uranium (λ = 279.394 and 329.133 nm), ruthenium (λ = 240.272 and 267.876 nm), rhodium (λ = 252.053 and 249.077 nm) and palladium (λ = 324.270 and 229.651 nm). ICP-AES analyses were calibrated by using several uranium and PGM solutions prepared by diluting a certified standard 1000 ppm solution in a 0.2 mol.L^{-1} HNO_3 solution. The elemental concentrations in solution were determined from the average concentration of three replicates. Otherwise, ICP-AES showed an increase of the PGM detection limit in the presence of uranium. Indeed, the PGMs detection limits obtained for this analytical protocol were 10^{-1} ppm in the presence of uranium in the solution and 10^{-2} ppm in its absence. This effect of uranium in solution can be explained by interferences between the emission spectra of the elements and by the greater amount of uranium solubilized compared to PGMs due to the composition of the sample.

Structural characterization was carried out by PXRD using a Bruker D8 Advance diffractometer (LynxEye detector) in the reflection geometry with Cu Kα1,2 radiation (λ = 1.5418 Å). The data were collected at room temperature in an angular range of 5° < 2θ < 100°, with a step of 0.0167° and a total counting time of about 3 hours. Using the Thompson-Cox-Hastings pseudo-Voigt profile function implemented[40] in the FullProf Suite program[41], all of the PXRD patterns were refined using the Rietveld method. The conventional profile/structure parameters such as zero shift, unit cell parameters, scale factors, global thermal displacement and asymmetric parameters were allowed to vary during all of the refinements. For each phase, the intrinsic microstructure parameters were modeled by applying an anisotropic size model.

After the sintering step, the density of the pellets was determined by geometric measurements using a caliper splint and by ethanol pycnometry. Geometric measurements gave access to the densification rate, whereas ethanol pycnometry was performed to discriminate between total, open and closed porosities as described in a previous paper[27].

Moreover, the morphological characterization of the samples was performed by SEM with an FEI Quanta 200 environmental scanning electron microscope using a back-scattered electron detector (BSED) or a secondary electron detector (SED) in vacuum conditions with an acceleration voltage of 25 kV. SEM micrographs recorded at low magnification were also used to evaluate the initial specific surface area (S_{SA} in $m^2.g^{-1}$) of the pellets as already described in previously published works[27, 42]. Briefly, five images measuring 92 µm × 62 µm were binarized using Fiji software[43] to determine the surface area of the pores visible in the zone observed by SEM. The pore diameter distribution was evaluated from these images using the "analyze particles" plug-in implemented in Fiji. Next, the surface area linked to the pores was calculated assuming that the pore size distribution of the analyzed domain was representative of the entire sample and that the pores were cylindrical. The resulting surface area of the pores was then weighted by the fraction of open porosity deduced from geometric and pycnometric density measurements. For each sample, an average specific surface area value was deduced from the analysis of the five images recorded at low magnification.

In order to highlight the influence of the presence of PGMs on the UO_2 dissolution kinetics, the results obtained in the presence of PGMs particles were compared to those obtained with the pure UO_2 sample used as a reference[27].

3. Dissolution experiments

a. Dissolution conditions and protocol for monitoring the solid/liquid interface by ESEM

Dissolution tests were performed in static conditions using polytetrafluoroethylene containers placed in an oven at 60°C under stirring at 200 rpm. For these tests, pellets of 150 to 200 mg were put into contact with 25 mL of 0.1 $mol.L^{-1}$ HNO_3 solution for a few hours to several weeks. These conditions were chosen based on the multiparametric study of the dissolution of UO_2 performed previously[27]. Indeed, the induction period for the dissolution of UO_2 in the absence of PGMs particles was found to be 120 days in a 0.1 $mol.L^{-1}$ HNO_3 solution at 60°C. Under these conditions, the catalyzed UO_2 dissolution reaction is not expected to become the predominant mechanism before a very long time period has passed, so an acceleration of the dissolution can be attributed only to the presence of the PGMs particles.

After a given time, the sample was removed from the dissolution bath, and then washed three times with water and finally once with ethanol, in order to halt the dissolution reaction. During this time, a 2-mL aliquot was removed and then replaced by the same volume of fresh nitric acid solution

to maintain a constant volume of solution. Depending on the solution considered, *i.e.*, on the concentration of uranium released, the aliquots were diluted with 0.2 mol.L^{-1} HNO_3 solution. Uranium and PGMs elemental concentrations were then determined using ICP-AES, as detailed previously.

At the same time, the sample was introduced into the ESEM chamber, with special attention being paid to sample dehydration during this step. The ESEM chamber was equipped with a Peltier stage, and a specific pumping sequence was used to slowly replace the air with water vapor and to finally maintain the sample under wet conditions. Next, two regions of interest were selected, and micrographs were recorded at various magnifications and with three tilt angles (-10°; 0°; +10°). The surface area of each of these two investigated zones was S_{image} = 552 µm². ESEM-optimized images were recorded using the conditions optimized by Podor et al.[38]: working distance = 6 mm; acceleration voltage = 6 kV; spot size = 3 – 4; diaphragm diameter = 20 µm; image acquisition conditions = 2048 × 1887 pixels with 1 µs per pixel and accumulation of 16 images with drift correction; and magnification = ×20000, ×10000, ×5000 (corresponding to 6.35 µm × 5.482 µm, 12.7 µm × 10.974 µm and 25.4 µm × 21.927 µm fields of view, respectively). After this observation step, the sample was once again immersed in the dissolution bath. This sequence was repeated until the investigated regions disappeared.

ESEM images recorded at different dissolution times were aligned and compiled in a stack of images. The visualization of the stack enabled qualitative monitoring of the microstructural changes occurring at the solid/solution interface.

b. 3D reconstructions and height map

ESEM images were recorded with three tilt angles (-10°; 0°; 10°). The 3D reconstruction of the surface of the investigated domains was performed using commercial Alicona MeX software and the three stereoscopic images. A 16-bit height map was extracted from the 3D surface reconstruction using a scale of 1 Å per pixel (corresponding to the grey scale). Height maps obtained for various dissolution times were compiled in a stack. The height maps were aligned twice, alternately using the Linear Stack Alignment with SIFT[44] and StackReg[45] plug-ins with Fiji software. These height maps were the raw material used to characterize the variations of the sample topography with dissolution time.

The ratio between the surface area of the 3D reconstructions and the surface area of the investigated domain (S_{micro}/S_{image}) was calculated by the Alicona MeX software. This made it possible to estimate the evolution of the surface area of the zones investigated by ESEM during dissolution.

Furthermore, the Alicona MeX software was used to determine the amount of matter dissolved locally from each dissolution time considered to the next. The Abbott-Firestone curve (or bearing area curve) was used to describe the texture of the reconstructed surface of the sample[46]. From this curve,

the void core volume (V_{vc} in $cm^3.m^{-2}$) was calculated. By considering that the surface of the sample was flat prior to the dissolution test and assuming that the highest points of the reconstructed surface corresponded to the initial surface, the V_{vc} was considered to be the cumulative volume of matter dissolved. This volume was then multiplied by the density of the material (11 $g.cm^{-3}$ in the case of UO_2) to estimate the dissolved mass.

The spatial distribution of the dissolved matter was determined by the difference between the height maps obtained for different dissolution times. The height map differences were then represented in a 3D view using the "3D surface" Fiji software tool, thereby bringing preferential dissolution zones to light.

The evolution of the depth and width of the grain boundaries was quantified using the stack of height maps and the "plot profile" tool of the Fiji software. Three grain boundaries were chosen on the first height map, and a profile 0.9 µm long and 102 nm wide was drawn perpendicular to them. In order to enable the comparison of height profiles, it was necessary to define a reference height. This reference height was chosen by considering one detail that always remained recognizable from one height map to the next. Using the corrected height map profiles, the dissolution rate of the grain boundaries was derived. Indeed, the integration of the corrected height profile led to the surface area of the cross-section of the grain boundary. This surface area multiplied by the profile width (102 nm) corresponded to the volume of dissolved material at the grain boundary (Figure 1). This volume was multiplied by the density of the material (11 $g.cm^{-3}$ in the case of UO_2) to estimate the mass of dissolved material at the grain boundary.

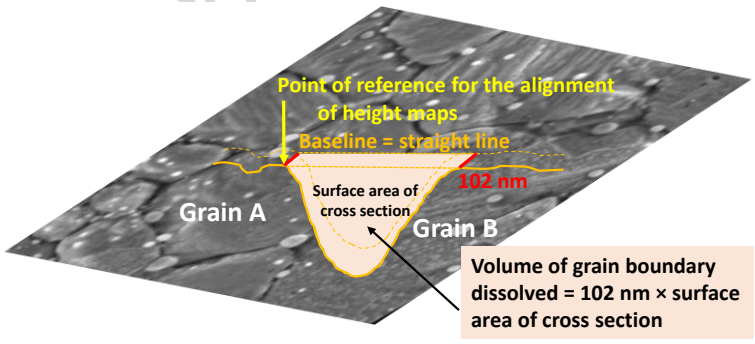

Figure 1. Evaluation of the volume of dissolved material from the height profile drawn perpendicular to the grain boundary.

c. *Determination of macroscopic and microscopic normalized dissolution rates*

The ICP-AES analyses of the aliquots sampled from the dissolution solution made it possible to determine the evolution of the elemental concentrations in solution. The mass of UO_2 dissolved at time t, $\Delta m(t)$ (in wt.%) was calculated from the ICP-AES measurements as follows:

$$\Delta m(t) = \frac{m_U(t)}{f_U \times m_0} \times 100 = \frac{C_U(t) \times V}{f_U \times m_0} \times 100 \quad (1)$$

where $m_U(t)$ (g) corresponds to the mass of uranium released in the solution at time t calculated from the elemental concentration, $C_U(t)$ (g.L^{-1}) and the volume of solution in contact with the solid, V (L); f_U (= 0.88 g.g^{-1}) is the mass fraction of uranium in UO_2 and m_0 is the initial mass of the pellet (g).

In accordance with the literature, the normalized weight loss, N_L(U, t) (g.m^{-2}), was calculated from the elemental concentration as follows:

$$N_L(\mathrm{U},t) = \frac{m_U(t)}{f_U \times S(t)} = \frac{m_U(t)}{f_U \times S_{SA} \times \left(m_0 - \frac{m_U(t-1)}{f_U}\right)} \quad (2)$$

where $S(t)$ (m²) is the surface area of solid in contact with the solution at time t, and S_{SA} (m².g^{-1}) is the initial specific surface area of the pellet. It is worth noting that in equation (2) the specific surface area of the pellet is considered to remain constant.

From the analysis of the 3D reconstructions of the solid/solution interface, the normalized weight loss, $N_L^{micro}(\mathrm{U},t)$ (g m^{-2}), was also calculated at the microscopic scale as follows:

$$N_L^{micro}(\mathrm{U},t) = \frac{\left(V_{VC}(t) - V_{VC}(t=0)\right) \times d_{UO2}}{S_{micro}(t)} \quad (3)$$

where V_{VC} (cm^3) and S_{micro} (m²) correspond to the void core volume and the surface area of the solid/solution interface, respectively, both of which were calculated by the Alicona MeX software from the 3D reconstructions of the ESEM micrographs, and d_{UO2} (= 11 g.cm^{-3}) is the density of uranium dioxide.

The normalized dissolution rates, R_L(U,t) (g.m^{-2}.d^{-1}), were derived from the evolution of the normalized weight loss following:

$$R_L(\mathrm{U},t) = \frac{d\,N_L(U,t)}{d\,t} \quad (3)$$

3. Results and discussion

1. UO_2 + PGMs pellets characterization

The UO_2 pellets doped with PGMs (Ru, Rh, Pd) were characterized prior to the dissolution experiments. First of all, the synthesis yield was determined by ICP-AES analysis of the elemental concentrations remaining in the supernatant separated from the freshly-precipitated precursor by centrifugation. The concentrations of Ru, Rh and Pd in the supernatant were below the detection limits of the ICP-AES apparatus. The precipitation yield was thus calculated using the concentration of uranium in solution and was found to be higher than 99%. Next, the composition of the synthesized uranium oxide powder doped with PGMs was also determined after complete dissolution of the solid. The molar fraction of each element in the powder (Table 1) was not significantly different from that which was expected, meaning that the precipitation of uranium and PGMs via the hydroxide route was

quantitative. The sample composed of 97 mol.% uranium and 3 mol.% PGMs is hereinafter noted UO_2 + 3 mol.% PGMs.

Table 1: Obtained molar fraction vs. expected molar fraction of uranium and each PGM of interest determined by ICP-AES analyses.

Elements	Expected molar fraction	Obtained molar fraction
U	0.97	0.97 ± 0.06
PGM	0.03	0.03 ± 0.02
Rh	0.016	0.016 ± 0.003
Pd	0.003	0.003 ± 0.001
Ru	0.011	0.011 ± 0.002

Powder X-ray diffraction analysis was carried out for the powder prepared by thermal conversion of the hydroxide precursor (Figure S1 of the supplementary data). The PXRD pattern showed only the peaks characteristic of the UO_2 structure ($Fm\bar{3}m$ space group). The molar fraction of PGMs in the powder was too low for any additional phase to be detected in the UO_2. Rietveld refinement of the PXRD pattern led to a = 5.470 ± 0.001 Å, in good agreement with the cell parameter value usually reported for nearly-stoichiometric UO_2: a = 5.468 ± 0.001 Å[47]. This result indicated that the PGMs were not incorporated into the UO_2 fluorite structure.

Pellets were obtained after shaping followed by a sintering step performed for 8 hours at 1500°C under reducing atmosphere (Ar + 5% H_2). The microstructural properties of the UO_2 and UO_2 + PGMs pellets used in this study are summarized in Table 2.

Table 2: Densification rates of the sintered pellets used in the dissolution experiments calculated from geometric and pycnometric measurements (expressed in %), closed porosity and open porosity values, and specific surface area determined from SEM image analysis. The uncertainties correspond to twice the standard deviation calculated from five measurements.

Sample	m (t = 0) (g) ± 0.001	Geometric densification rate (%)	Pycnometric densification rate (%)	Closed porosity (%)	Open porosity (%)	Specific surface area ($m^2.g^{-1}$)
UO_2 + PGMs	0.199	90 ± 1	92 ± 1	8 ± 2	2 ± 2	(3.2 ± 0.6) × 10^{-3}
UO2	0.207	89 ± 1	91 ± 1	9 ± 2	1 ± 2	(6.7 ± 2.0) × 10^{-3}

The microstructure of the prepared UO_2 and UO_2 + 3 mol.% PGMs pellets is compared to a real spent MO_x fuel (45 $GWd.t^{-1}$)[48] in Figure 2. The microstructure of the UO_2 + 3 mol.% PGMs pellet (Figure 2 (b)) was similar to that of UO_2 (Figure 2 (a)), except that light grey spherical particles of less than 100 nm in diameter appeared at the surface of UO_2 grains and at the grain boundaries. Energy-dispersive X-ray spectroscopy (X-EDS) analyses of the prepared sample showed that the light grey particles were composed of Ru, Rh and Pd alloys (bi- or trimetallic alloys) of variable composition. Furthermore, the presence of Ru, Rh or Pd in UO_2 matrix was not detected by X-EDS. These metallic

particles were mainly located at the grain boundaries, whether at the surface or in the bulk material, as already described in the real SNF (Figure 2 (c) shows an intergranular fracture). The microstructure obtained for the prepared pellets was thus similar to that of the real spent nuclear fuel, except that the UO_2 grains were smaller.

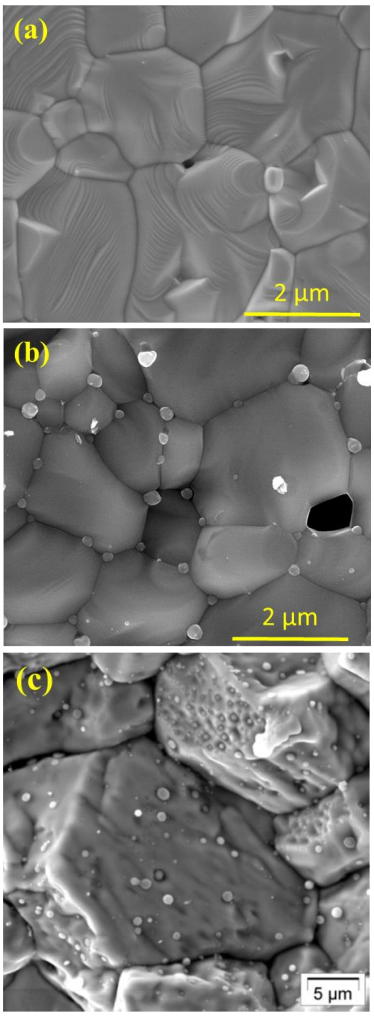

Figure 2: SEM micrographs of UO_2 (a); UO_2 + 3 mol.% PGMs (b) pellets; and intergranular fracture in a real spent nuclear fuel (c)[48].

2. Dissolution results obtained at the macroscopic scale

The evolution of the relative mass loss $\Delta m(U,t)/m_0$ (%) of the UO_2 and UO_2 + 3 mol.% PGMs pellets during dissolution in 0.1 mol.L^{-1} HNO_3 at 60°C, determined by successive ICP-AES analyses of the dissolution medium, is presented in Figure 3. The evolution of the relative mass loss was determined with and without ESEM monitoring of the solid/solution interface for the UO_2 + 3 mol.% PGMs pellets in order to bring to light any potential impact of the monitoring protocol on the dissolution rate. In 0.1 mol.L^{-1} HNO_3, both curves were superimposed over a period of 12 days (corresponding to a relative mass loss of less than 2%). After that point, the dissolution rate obtained in the absence of monitoring increased. For example, a mass loss of 25% was determined after 54 days

of dissolution with monitoring, whereas this value was reached after only 30 days without monitoring. This discrepancy indicates that the protocol used, which required to stop the dissolution experiment regularly, modified the kinetics of dissolution of the UO_2 + 3 mol.% PGMs pellets, leading the dissolution rate to decrease by almost a factor of two. It is, however, important to note that part of this discrepancy could be also explained by sample variability. Nevertheless, the shape of the curves characterized by an increase of the dissolution rate after 20 days was found to be similar with and without ESEM monitoring. This result indicates that even if the kinetics changed, the underlying dissolution mechanism remained the same. As expected, the presence of the PGMs particles strongly increased the dissolution rate even with ESEM monitoring of the solid/solution interface. For example, the relative mass loss of UO_2 determined after 237 days of dissolution in 0.1 mol.L^{-1} HNO_3 at 60°C (2.5%) was reached after 15 days for UO_2 + 3 mol.% PGMs. It is noteworthy that Cordara et al.[27] reported a 1.3% relative mass loss for UO_2 in 270 days without ESEM monitoring, which was lower than the value observed with monitoring in this study.

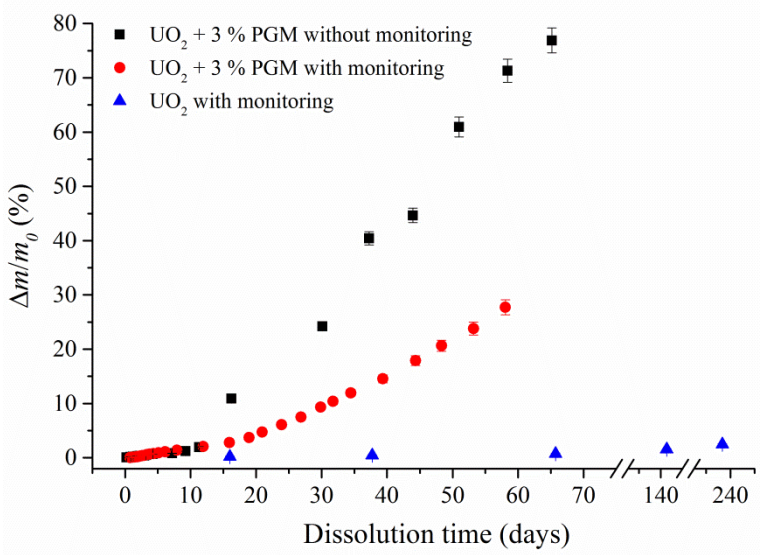

Figure 3: Evolution of the relative mass loss $\Delta m(U,t)/m_0$ of UO_2 (blue triangles) and UO_2 + 3 mol.% PGMs pellets with (red dots) or without (black squares) *operando* monitoring in 0.1 mol.L^{-1} HNO_3 at 60°C.

3. Qualitative monitoring of the evolution of the solid/solution interface during dissolution

Each data point reported in Figure 3 was associated with the observation of the surface of the pellets by ESEM. Some of the ESEM micrographs recorded during the dissolution of UO_2 + 3 mol.% PGMs and UO_2 pellets in 0.1 mol.L^{-1} HNO_3 solution at 60°C are presented in Figure 4 (a) and (b), respectively. The surface area of the ESEM micrographs in Figure 4 was 6×6 µm².

The microstructural evolution of UO_2 + 3 mol.% PGMs and UO_2 pellets in 0.1 mol.L^{-1} HNO_3 solution was completely different, even when the relative mass loss was comparable. The relative mass loss of the UO_2 pellet in Figure 4 (b-5) was 2.47%, a value close to that determined for UO_2 + 3

mol.% PGMs in Figure 4 (a-3). At this stage, however, the initial microstructure of the UO_2 pellet was only slightly modified in the investigated zone, through smoothing at the surface of the grains and enlargement of the pores, whereas grain boundaries were not specifically attacked.

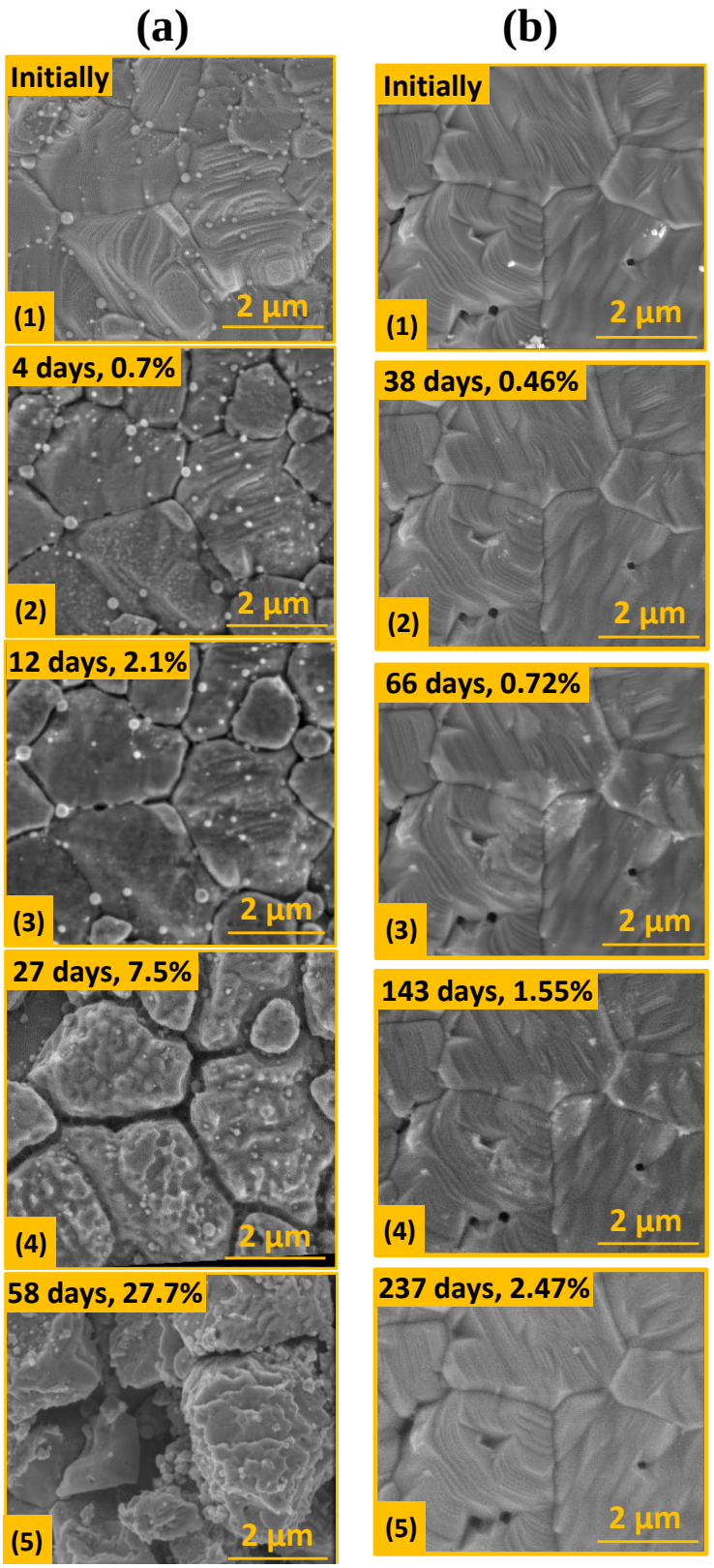

Figure 4: ESEM micrographs recorded at different times during dissolution of UO_2 + 3 mol.% PGMs (a) and UO_2 (b) pellets in 0.1 mol.L^{-1} HNO_3 at 60°C. The associated relative mass loss $\Delta m(U,t)/m_0$ (%) determined at the macroscopic scale is indicated in the yellow header of each image.

The sequence of images for UO_2 + 3 mol.% PGMs in Figure 4 (a) shows that the dissolution was located mainly at the grain boundaries prior to 12 days of dissolution in 0.1 mol.L^{-1} HNO_3, corresponding to a relative mass loss of 2.1% (Figure 4 (a-3)). The following micrograph, recorded after 27 days (and 7.5% relative mass loss), shows massive dissolution of UO_2 grains characterized by a significant decrease in their size and an increase in their roughness. This phenomenon finally led to the disappearance of some grains and the loss of the initial microstructure (Figure 4 (a-4) and (a-5)). It is noteworthy that the micrographs presented in Figure 4 (a-4) and (a-5) were recorded after the increase of the dissolution rate observed at the macroscopic scale (Figure 3). Also, PGMs particles were always visible in the sequence of images recorded during the dissolution in 0.1 mol.L^{-1} HNO_3, but their number seemed to decrease.

Figure 5 shows a micrograph of the surface of UO_2 + 3 mol.% PGMs pellet after 21 days in 0.1 mol.L^{-1} HNO_3 solution at 60°C. It appears that in most locations, the dissolution of the grains was enhanced in the vicinity of the PGMs particles. This is particularly true at the grain boundaries (yellow circles in Figure 5), but also, to a lesser extent, at the surface of the grains.

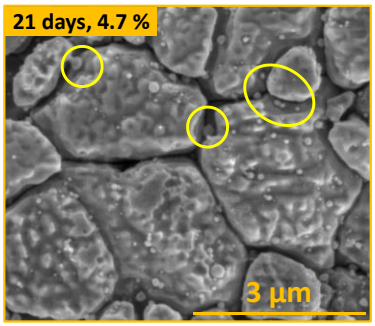

Figure 5: ESEM micrograph of UO_2 + 3 mol.% PGMs pellet recorded after 21 days of dissolution in 0.1 mol.L^{-1} HNO_3 at 60°C. The yellow circles indicate typical preferential dissolution zones around PGMs particles.

This specific dissolution could be explained by an accumulation of reactive species catalyzing UO_2 dissolution close to the metallic particles. Indeed, PGMs particles could reduce NO_3^- ions to HNO_2 in nitric acid solution, which is known to increase the oxidative dissolution rate of UO_2[28-32, 49]. Once present in solution, HNO_2 could accumulate in fractures, holes and pores in which the solution is slowly renewed through transport phenomena. This mechanism could explain the strong increase in the dissolution rate of UO_2 in the presence of PGMs particles and the formation of preferential dissolution zones in the vicinity of PGMs particles. When one considers the standard reduction potentials of Ru^{2+}/Ru (E° = 0.455 V/NHE), Rh^{+}/Rh (E° = 0.600 V/NHE) or Rh^{3+}/Rh (E° = 0.758 V/NHE), and NO_3^-/HNO_2 (E° = 0.934 V/NHE), it becomes clear that these metals are able to reduce nitrate ions. Nevertheless, this is not the case for palladium (with E° (Pd^{2+}/Pd)= 0.951 V/NHE)[34]. This mechanism also involves the dissolution of the PGMs particles. It is always possible to observe some

metallic particles in the sequence of ESEM images presented in Figure 4 (a), though the number of observable PGMs particles varies with time. Several phenomena apart from dissolution could, however, affect this number. First of all, the rapid dissolution of UO_2 grains leads to the release of PGMs particles trapped in the grain boundaries. Then, the free PGMs particles could either accumulate at the solid/solution interface or be released into the bulk solution through mechanical stirring of the dissolution medium. Therefore, ESEM images alone do not permit a conclusion about the dissolution rate of the PGMs particles. The ICP-AES analyses of the elemental concentrations of Pd, Ru and Rh in solution were also inconclusive, due to interferences with uranium, which was present at a much higher concentration in solution than the PGMs.

4. Quantitative monitoring of pellet microstructure changes during dissolution

For the first time, the recording of successive stereoscopic ESEM micrographs associated with the use of Alicona MeX software made it possible to perform a quantitative analysis of the microstructural evolution of the solid/solution interface during dissolution. This analysis was carried out for the UO_2 + 3 mol.% PGMs pellet dissolved in 0.1 mol.L^{-1} HNO_3 at 60°C. Indeed, numerous images were recorded under these conditions, with pellet dissolution progressing significantly until 28% relative mass loss was attained. In addition, the heterogeneous evolution of the microstructure of the pellet under these conditions allowed to obtain better 3D reconstruction accuracy. Indeed, Podor et al.[38] showed that the greater the height differences at the surface of the pellet, the smaller the errors on the height maps. A selection of ESEM images recorded in the zone of interest at the surface of UO_2 + 3 mol.% PGMs pellet dissolved in 0.1 mol.L^{-1} HNO_3 at 60°C, with a tilt angle of 0° and at the highest magnification, is provided in Figure S2. The corresponding height maps (in shades of grey) obtained with Alicona MeX software using three stereoscopic images (tilt angles = -10°, 0°, +10°) are also reported.

For UO_2 pellet dissolved under the same conditions, the dissolution did not sufficiently modify the topography of the grains, and the solid/solution interface remained flat in the zone investigated. This kind of topographic evolution was unsuitable for 3D reconstruction.

a. Macroscopic vs. microscopic normalized weight loss

Thanks to the Alicona MeX software, for each 3D reconstruction it was possible to determine the surface area developed by the solid/solution interface in the investigated zone during dissolution. These values corresponded to the topographic surface area developed by the 3D reconstruction. Figure 6 shows the evolution of the ratio between the surface area developed by the 3D reconstruction (true area) and the surface area of the reconstructed zone (projected area) during the dissolution of UO_2 + 3 mol.% PGMs pellets in 0.1 mol.L^{-1} HNO_3 at 60°C. To test the reproducibility of the method, these data were calculated for two sequences of images recorded in the zone of interest at two different magnifications. Thus, the projected area of the ESEM images varied from 11 × 11 µm² for the highest

magnification to 22 × 22 µm² for the lowest magnification. In this representation, a ratio of one corresponds to a perfectly flat surface.

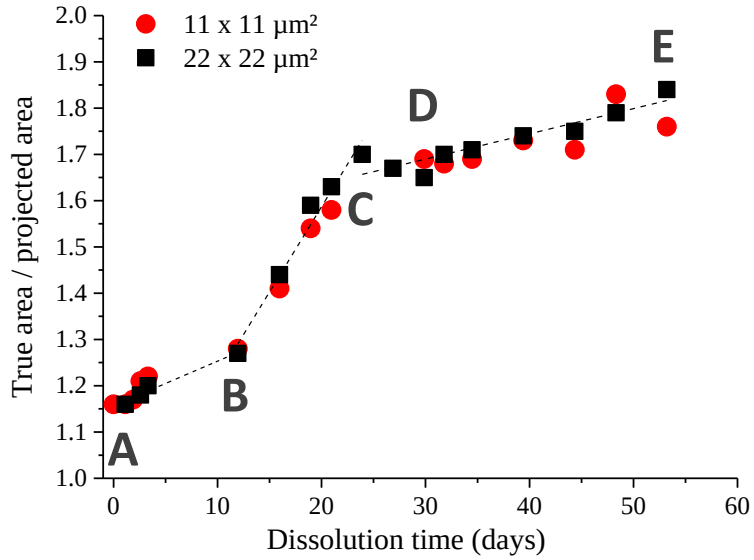

Figure 6: Evolution of the ratio between the surface area developed by the 3D reconstruction obtained with Alicona MeX software (true area) and the surface area of the reconstructed zone (projected area) for two sequences of images recorded at two different magnifications during the dissolution of UO_2 + 3 mol.% PGMs pellet in 0.1 mol.L^{-1} HNO_3 at 60°C. Dissolution times noted A, B, C, D and E correspond to the ESEM images presented in Figure S2.

A significant evolution of the ratio between the true area and the projected area is clearly highlighted in Figure 6. At the end of the experiment ($\Delta m/m_0$ = 28 %), the dissolution of the pellet led to an increase of the true surface area by a factor of 1.80 ± 0.04. This increase occurred in three steps. The first step between images A (t = 0.8 day) and B (t = 12 days), as well as the third step between images D (t = 30 days) and E (t = 53 days), corresponded to a low rate of increase. During the second step, between images B (t = 12 days) and D (t = 30 days), the surface area increased more rapidly. By examining the sequence of ESEM images in Figure S2, one can deduce that the initial increase of the surface area (between A, t = 0.8 day and B, t = 12 days), was linked to the dissolution of the grain boundaries. The strong increase in surface area between points B and C corresponded to the widening of the grain boundaries and to the increase of the roughness of the UO_2 grains caused by their dissolution. Between images D (t = 30 days) and E (t = 53 days), the evolution of the microstructure of the pellet appeared to be slow and essentially linked to the detachment of grains from the surface of the pellet, thereby contributing to a moderate increase of the surface area. In terms of the macroscopic relative mass loss of the pellet, the time period during which the surface area of the reconstructed zone was found to increase the fastest corresponded to relative mass losses of 2 to 9%. Fukasawa and Osawa[50] showed that at the beginning of the dissolution of UO_2 pellets in 7.4 N HNO_3 solution at 90°C, the effective surface area initially increases due to pore production, but subsequently decreases due to decreased pellet volume. Even if the mechanism of dissolution was probably different in their

case, Fukasawa and Osawa also showed that the increase of the effective surface area was time-limited.

Moreover, using the surface area (µm²), the void core volume of the 3D reconstruction (V_{VC} in cm^3) and equation (3), it was possible to calculate the normalized weight loss at the microscopic scale ($N_L^{micro}(U,t)$ in $g.m^{-2}$). The evolution of the microscopic normalized weight loss was calculated for the two sequences of ESEM images recorded at two different magnifications. The results obtained at the microscopic scale from the 3D reconstructions of the solid/solution interface, along with the evolution of the macroscopic normalized weight loss calculated from the elemental uranium concentration in solution during dissolution of the pellet, are compared in Figure 7.

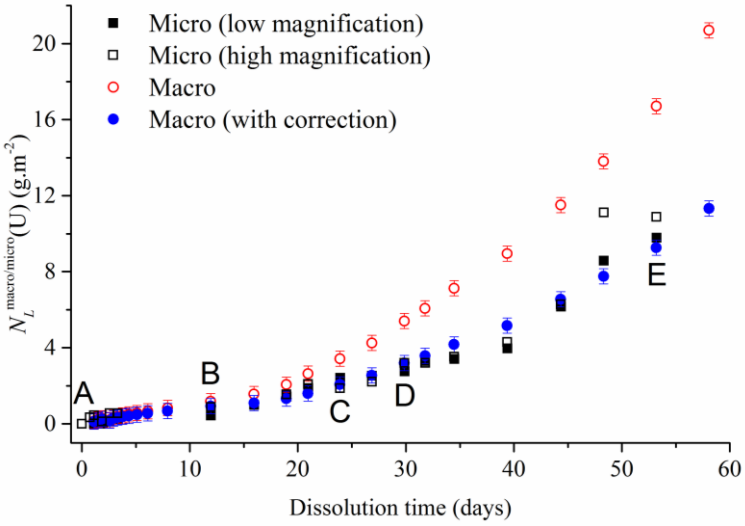

Figure 7: Evolution of the normalized weight loss, N_L^{micro} (U) ($g.m^{-2}$), calculated using the true surface area and the void core volume of 3D reconstructions of the solid/solution interface by Alicona MeX (■ low magnification and □ high magnification), of the normalized weight loss N_L^{macro}(U) ($g.m^{-2}$) calculated from elemental U concentration in solution and the initial specific surface area of the pellet (○) and of the normalized weight loss N_L^{macro}(U) ($g.m^{-2}$) after a correction taking into account the evolution of the specific surface area (●) during dissolution of UO_2 + 3 mol.% PGMs pellet in 0.1 $mol.L^{-1}$ HNO_3 at 60°C.

The dissolution curves determined at the macroscopic and microscopic scales presented in Figure 7 exhibited a similar shape. An increase in the dissolution rate was observed after 20 days of dissolution at both the micro- and macroscopic scales. From 20 days to the end of the experiment, however, the macroscopic normalized weight loss remained higher than its microscopic counterpart. Assuming that this discrepancy could be explained by the evolution of the surface area of the pellet, the macroscopic weight loss was corrected using the results presented in Figure 6. Contrary to what was done previously, the specific surface area S_{SA} in equation (2) was assumed to vary with the dissolution time. The value of S_{SA}(t) was thus estimated by multiplying the initial specific surface area of the pellet by the ratio of the true area over the projected area determined at time *t* with Alicona MeX. The evolution of the N_L^{macro}(U) calculated using the effective surface area of the pellet is plotted in Figure 7. After applying this correction taking into account the evolving surface area of the pellet, the macroscopic and microscopic weight losses were not significantly different. This correction shows

that a significant contribution to the increase of the normalized dissolution rate observed at the macroscopic scale was in fact caused by the underestimation of the effective surface area of the pellet. In addition, these results show that for a given zone that is representative of the pellet, ESEM monitoring makes it possible to determine an accurate dissolution rate at the local scale and to eliminate issues associated with the quantification of the effective surface area of the sample at the macroscopic scale.

b. Preferential dissolution zones

As described in the experimental section, it was possible to subtract height maps obtained at different dissolution times in order to map the dissolved volumes. The volumes of UO_2 dissolved between 0.8 and 12 days, 29.9 days, and 53.2 days in 0.1 mol.L^{-1} HNO_3 at 60°C and in the presence of 3 mol.% PGMs particles are presented in Figure 8.

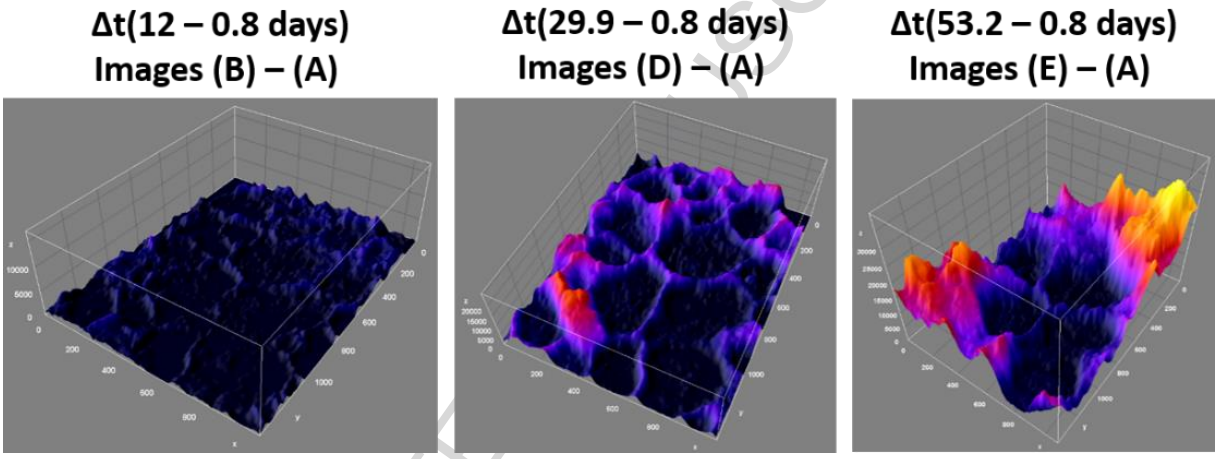

Figure 8: Volume of matter dissolved obtained by subtracting height maps recorded at different dissolution times during the dissolution of UO_2 + 3 mol.% PGMs pellet in 0.1 mol.L^{-1} HNO_3 at 60°C. The dissolution time of 0.8 day corresponds to the first 3D reconstruction achievable with the Alicona MeX software.

These maps highlight the preferential dissolution of the grain boundaries, in particular prior to 29.9 days of dissolution (D-A). This analysis confirms that the fast increase of the surface area (Figure 6) was mainly caused by the opening of grain boundaries for this material. The difference between the height maps obtained after 0.8 and 53 days of dissolution also demonstrates the detachment of grains as a consequence of the dissolution of the grain boundaries.

The height maps of the zone of interest obtained at various dissolution times (Figure S2) were aligned and compiled with the Fiji software. The ESEM image of the zone of interest with the localization of the selected profiles is shown in Figure 9 (a). Three of these profiles were drawn perpendicularly to the grain boundaries (GB #i), and one of them was drawn longitudinally (TJ). The evolution of the height profiles GB #1 and TJ are plotted in Figure 9 (b) and (d), respectively. The 3D plot of the grain boundaries and of the triple junctions TJ is presented in Figure 9 (c). The evolutions of the height profiles GB #2 and GB #3 are presented in Figure S3 of the supporting information.

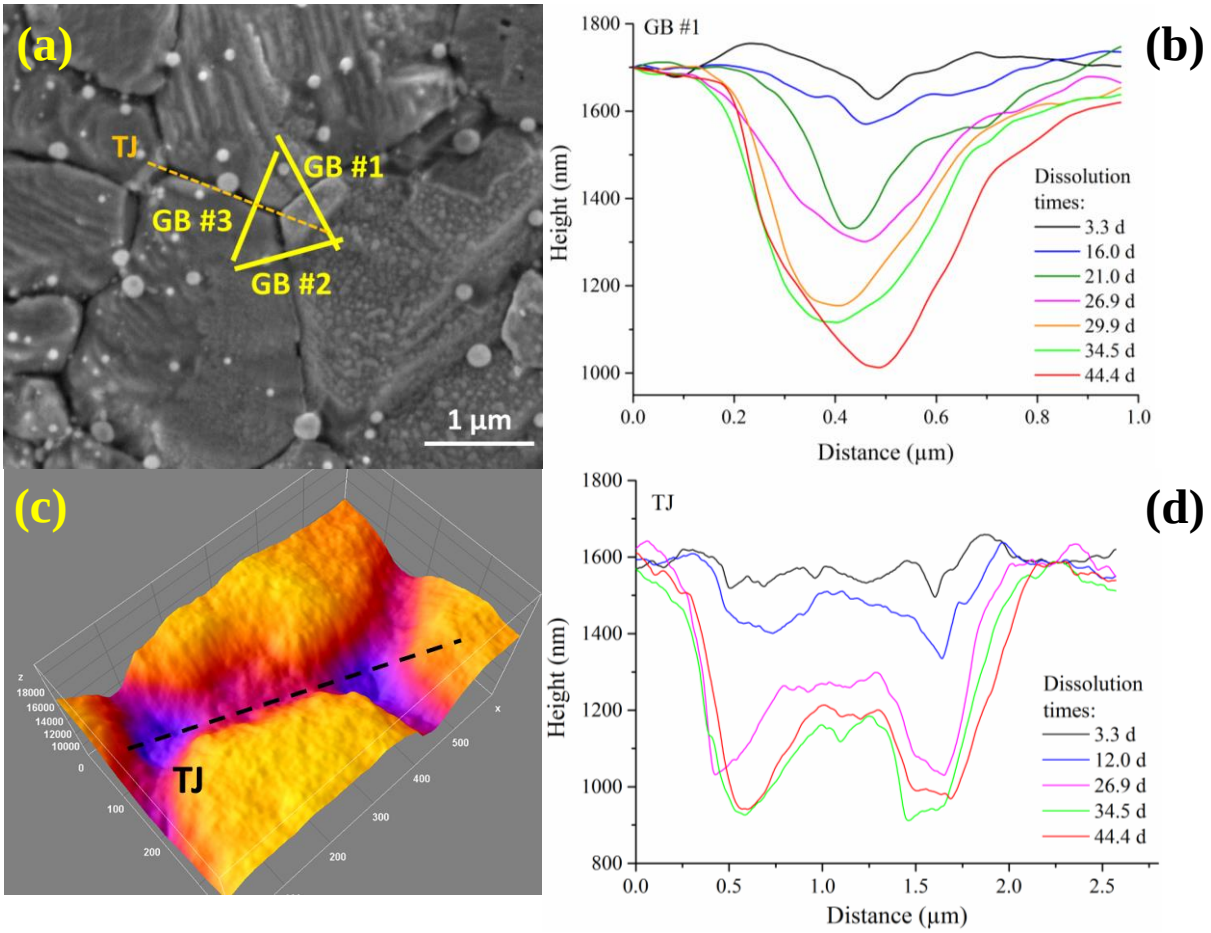

Figure 9: ESEM image of the zone of interest showing the localization of the four height profiles (a); evolution of the height profiles GB #1 (b); 3D plot of the grain boundaries and of the triple junctions TJ after 26.9 days of dissolution (c); and evolution of the height profiles TJ (d) during the dissolution of UO_2 + 3 mol.% PGMs pellet in 0.1 mol.L^{-1} HNO_3 at 60°C.

The height profiles presented in Figure 9 (b) show that the depth and width of grain boundary GB #1 increase as the dissolution progresses. In Figure 9 (b), it appears that the dissolution was initiated at the grain boundary, and was then quickly extended to the border of the adjacent grains. The depth of the grain boundary at the end of the dissolution test reached 650 to 700 nm, whereas its width was about 200 nm. After 34.5 days of dissolution, the depth of the grain boundaries increased more slowly. Because of the size of the grains of UO_2, the underlying grain might have been attained at this stage. The preferential dissolution of the triple junctions is also highlighted in Figure 9 (c) and (d).

c. Determination of local dissolution rates

The volume of matter dissolved at the grain boundaries was calculated using the height profiles (Figure 9 (b) and Figure S3) following the method described in Figure 1. The evolution of the normalized weight loss of the grain boundaries is compared to the microscopic $N_L^{micro}(U)$ (g.m^{-2}) calculated using the 3D reconstructions of the whole image in Figure 10.

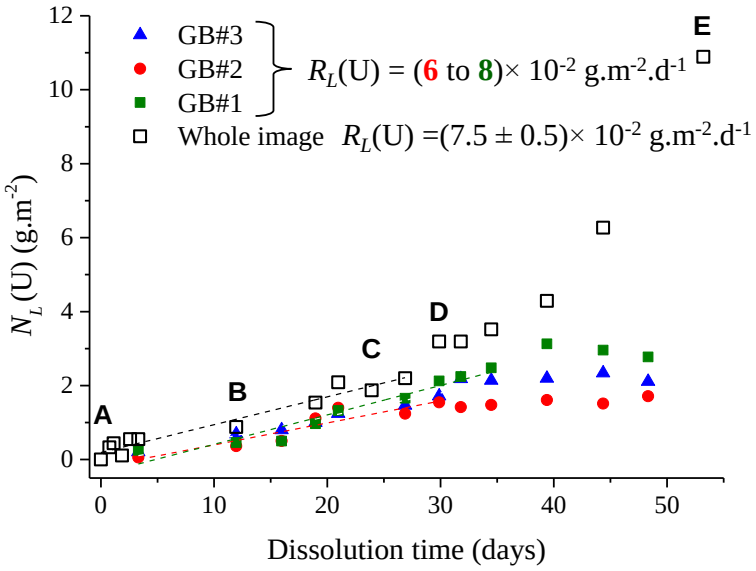

Figure 10: Evolution of the normalized weight loss N_L (U) (g.m^{-2}) determined at each grain boundary using the height profiles and using the 3D reconstruction of the whole ESEM image during the dissolution of UO_2 + 3 mol.% PGMs pellet in 0.1 mol.L^{-1} HNO_3 at 60°C. The normalized dissolution rate R_L(U) (g.m^{-2}.d^{-1}) was calculated in the linear part of the curves.

The normalized weight losses determined for the three selected grain boundaries followed a similar trend. At the beginning, the normalized weight loss increased linearly before reaching a constant value after 30 - 35 days of dissolution. The normalized dissolution rates of the three grain boundaries studied ranged from R_L(U) = (6 ± 1) × 10^{-2} to (8 ± 1) × 10^{-2} g.m^{-2}.d^{-1}. These values are not significantly different from the normalized dissolution rate determined for the whole image over the first 27 days of dissolution: R_L(U) = (7.5 ± 0.5) × 10^{-2} g.m^{-2}.d^{-1}. At the end of this step, the normalized dissolution rate calculated for the whole image increased, whereas the dissolution rate of the grain boundaries became negligible. This comparison shows that the dissolution of the whole pellet occurred mainly at the grain boundaries over the first 27 days (i.e., a macroscopic relative mass loss of 7.5%). Following this period, the increase of the roughness of the grains and the formation of corrosion pits contributed to the overall mass loss of the pellet. This normalized dissolution rate for the whole image for the first 27 days was also compared to the normalized dissolution rate of the non-catalyzed reaction determined by Cordara et al.[27] under the same conditions for UO_2: $R_{L,0}$(U) = (3.3 ± 0.1) × 10^{-3} g.m^{-2}.d^{-1}. In the presence of PGMs particles, the initial dissolution rate of the pellet increased by a factor of 23, leading to a strong shortening of the induction period (Figure 3).

Grain boundaries and triple junctions constitute preferential dissolution zones, as already observed for other ceramic materials[51-55]. The lower chemical durability of grain boundaries is generally explained by a slight difference of chemical composition compared to the bulk[56-58], or by a degraded crystalline order, even an amorphous state, as the junction between two crystals of different orientations leads to a high concentration of defects, especially for high misorientation angles[51]. That said, even if the presence of preferential attack sites (corrosion pits, cracks and pores) has already been

observed at various scales during the dissolution of UO_2 pellets in concentrated nitric acid solutions[35, 59-62], the opening of grain boundaries has not been clearly demonstrated until now. In particular, when Cordara et al. recorded a sequence of ESEM micrographs of UO_2 pellet dissolved in 1 M HNO_3 solution at 60°C, the dissolution was found to occur mainly through the normal retreat of the surface of the grains[27]. These observations underline the fact that the dissolution of UO_2 was initiated at the grain boundaries only in the presence of PGMs particles and at a low nitric acid concentration. This phenomenon could result from the localization of PGMs particles at the grain boundaries and from the accumulation of reactive species catalyzing the dissolution reaction in the space created between the grains. Depending on the rate of production of the reactive species, the rate of dissolution of the UO_2 grains and the diffusion rates of the species from and toward the bulk solution, the space between the grains could form, persist, enlarge or disappear.

4. Conclusion

The initial dissolution rate and the microstructural evolution of a UO_2 pellet incorporating 3 mol.% PGMs particles during dissolution in 0.1 mol.L^{-1} nitric acid solution at 60°C were found to be drastically different from those of a UO_2 pellet of similar initial microstructure. In the presence of PGMs particles, the initial dissolution rate of the pellet increased by a factor of 23, leading to a strong shortening of the induction period. In addition, the dissolution was heterogeneous at the surface of the pellet, with the development of preferential dissolution zones located at the grain boundaries where the PGMs particles were primarily located. Apart from the potential development of defects in the UO_2 structure due to the presence of the PGMs particles, several phenomena could explain these observations. First of all, the reduction of nitrate ions in nitric acid solution by metallic Ru and Rh particles to produce nitrous acid could cause a more rapid shift to the catalyzed reaction of dissolution of UO_2. Second, the dissolution of the PGMs particles, even at a low rate, leads to the production of aqueous PGMs species that are themselves oxidants for tetravalent uranium. In the absence of nitrous acid, the presence of these PGMs species in solution could increase the dissolution rate at the beginning of the dissolution process, thereby shortening the induction period before the catalyzed mechanism takes place. All of these reactions occurred at the interface between the metallic particles, the UO_2 and the solution. Thus, the accumulation of oxidants of UO_2 in the vicinity of the particles led to the appearance of preferential dissolution zones.

By using 3D-ESEM monitoring to observe how the topography of the solid/solution interface changed over time, it was possible to quantify the effective surface area of the UO_2 + 3 mol.% PGMs pellet during dissolution. This effective surface area increased over successive steps and was multiplied by a factor of 1.80 ± 0.04 at the end of the experiment (i.e., for a relative mass loss of $\Delta m/m_0$ = 28%). The increase in the specific surface area was one of the parameters responsible for the increase in the dissolution rate observed at the macroscopic scale. The normalized weight loss

calculated at the macroscopic scale from the elemental concentration of U in solution using the effective surface area determined at the microscopic scale made it possible to estimate an accurate value for the normalized dissolution rate. Moreover, microscopic normalized weight losses were calculated using the void core volume and the effective surface area of the 3D reconstructions. The values obtained were in very good agreement with the normalized weight losses determined at the macroscopic scale when the evolution of the effective surface area was taken into account. This result confirms the representativeness of the zone investigated by ESEM and illustrates the potential of this method for estimating the normalized dissolution rate of a material of a low and evolving specific surface area.

This multi-scale study paves the way toward various outcomes. First of all, in order to complete and confirm the UO_2 dissolution mechanism in the presence of PGMs particles, it is essential to measure the concentration and speciation of the PGMs in solution. To reach this goal, highly sensitive analytical techniques will be required. Second, the characterization of several UO_2 pellets incorporating various amounts of PGMs, whether alone or mixed, could enable the accurate determination of their distribution and speciation in the UO_2 matrix. Finally, the *operando* monitoring of the dissolution by 3D-ESEM sets the stage for the acquisition of new results in the domain of the dissolution of materials focusing on the "real" reactive surface area developed by the solid/solution interface as well as microscopic dissolution rates.

Acknowledgments:

The authors are grateful to Joseph Lautru (ICSM) and Béatrice Baus-Lagarde (ICSM) for their help in the ESEM and ICP-AES analyses, Julien Favrichon (CEA/STIC) for his participation in the choice of the 3D reconstruction software, and Murielle Bertrand (CEA/DMRC) and Stéphane Grandjean (CEA/DMRC) for helpful scientific discussions regarding the results obtained.

Supporting information:

The following figures are supplied as Supporting Information.

Figure S1: PXRD pattern of UO_2 + PGM recorded after crushing the sintered pellet, experimental data and pattern calculated using the Rietveld refinement method. Figure S2: ESEM images (tilt angle = 0°, highest magnification) of the zone of interest recorded at different times during the dissolution of UO_2 + 3 mol.% PGMs pellet in 0.1 mol.L^{-1} HNO_3 at 60°C. Reconstructed height maps obtained with Alicona MeX software associated with these images. Figure S3: Evolution of the height profiles GB#2 and GB#3 during the dissolution of UO_2 + 3 % mol. PGM pellet in 0.1 mol.L^{-1} HNO_3 at 60°C.

References

(1) Ewing, R. C. Long-term storage of spent nuclear fuel. *Nature Materials* **2015,** *14* (3), 252-257.
(2) Konings, R. J. M.; Wiss, T.; Benes, O. Predicting material release during a nuclear reactor accident. *Nat Mater* **2015,** *14* (3), 247-252, DOI: 10.1038/nmat4224.
(3) Bruno, J.; Ewing, R. C. Spent nuclear fuel. *Elements* **2006,** *2* (6), 343-349, DOI: 10.2113/gselements.2.6.343.
(4) Burns, P. C.; Ewing, R. C.; Navrotsky, A. Nuclear Fuel in a Reactor Accident. *Science* **2012,** *335* (6073), 1184-1188, DOI: 10.1126/science.1211285.
(5) Kleykamp, H. The chemical-state of the fission-products in oxide fuels. *Journal of Nuclear Materials* **1985,** *131* (2-3), 221-246, DOI: 10.1016/0022-3115(85)90460-x.
(6) Lewis, B. J.; Thompson, W. T.; Iglesias, F. C. 2.20 - Fission Product Chemistry in Oxide Fuels. In *Comprehensive Nuclear Materials*; Konings, R. J. M., Ed.; Elsevier: Oxford, 2012; pp 515-546.
(7) Buck, E. C.; Mausolf, E. J.; McNamara, B. K.; Soderquist, C. Z.; Schwantes, J. M. Nanostructure of metallic particles in light water reactor used nuclear fuel. *Journal of Nuclear Materials* **2015,** *461*, 236-243, DOI: https://doi.org/10.1016/j.jnucmat.2015.03.001.
(8) Cui, D.; Rondinella, V. V.; Fortner, J. A.; Kropf, A. J.; Eriksson, L.; Wronkiewicz, D. J.; Spahiu, K. Characterization of alloy particles extracted from spent nuclear fuel. *Journal of Nuclear Materials* **2012,** *420* (1), 328-333, DOI: https://doi.org/10.1016/j.jnucmat.2011.10.015.
(9) Thomas, L. E.; Einziger, R. E.; Woodley, R. E. Microstructural examination of oxidized spent pwr fuel by transmission electron-microscopy. *Journal of Nuclear Materials* **1989,** *166* (3), 243-251, DOI: 10.1016/0022-3115(89)90221-3.
(10) Poinssot, C.; Toulhoat, P.; Grouiller, J. P.; Pavageau, J.; Piron, J. P.; Pelletier, M.; Dehaudt, P.; Cappelaere, C.; Limon, R.; Desgranges, L.; Jegou, C.; Corbel, C.; Maillard, S.; Faure, M. H.; Cicariello, J. C.; Masson, M. *Synthesis on the long term behavior of the spent nuclear fuel.* ; CEA: 2001; p 304.
(11) Kleykamp, H.; Paschoal, J. O.; Pejsa, R.; Thummler, F. Composition and structure of fission-product precipitates in irradiated oxide fuels - correlation with phase studies in the Mo-Ru-Rh-Pd and BaO-UO_2-ZrO_2-MoO_2 systems. *Journal of Nuclear Materials* **1985,** *130* (FEB), 426-433, DOI: 10.1016/0022-3115(85)90329-0.
(12) Jiang, W.; Conroy, M. A.; Kruska, K.; Overman, N. R.; Droubay, T. C.; Gigax, J.; Shao, L.; Devanathan, R. Nanoparticle Precipitation in Irradiated and Annealed Ceria Doped with Metals for Emulation of Spent Fuels. *Journal of Physical Chemistry C* **2017,** *121* (40), 22465-22477, DOI: 10.1021/acs.jpcc.7b06188.
(13) Trummer, M.; Nilsson, S.; Jonsson, M. On the effects of fission product noble metal inclusions on the kinetics of radiation induced dissolution of spent nuclear fuel. *Journal of Nuclear Materials* **2008,** *378* (1), 55-59, DOI: http://dx.doi.org/10.1016/j.jnucmat.2008.04.018.
(14) Adachi, T.; Ohnuki, M.; Yoshida, N.; Sonobe, T.; Kawamura, W.; Takeishi, H.; Gunji, K.; Kimura, T.; Suzuki, T.; Nakahara, Y.; Muromura, T.; Kobayashi, Y.; Okashita, H.; Yamamoto, T. Dissolution study of spent PWR fuel - dissolution behavior and chemical-properties of insoluble residues. *Journal of Nuclear Materials* **1990,** *174* (1), 60-71, DOI: 10.1016/0022-3115(90)90421-i.
(15) Ikeuchi, H.; Sano, Y.; Shibata, A.; Koizumi, T.; Washiya, T. Dissolution behavior of irradiated mixed oxide fuel with short stroke shearing for fast reactor reprocessing. *Journal of Nuclear Science and Technology* **2013,** *50* (2), 169-180, DOI: 10.1080/00223131.2013.757466.
(16) Lausch, J.; Berg, R.; Koch, L.; Coquerelle, M.; Glatz, J. P.; Walker, C. T.; Mayer, K. Dissolution residues of highly burnt nuclear-fuels. *Journal of Nuclear Materials* **1994,** *208* (1-2), 73-80, DOI: 10.1016/0022-3115(94)90199-6.
(17) McNamara, B. K.; Buck, E. C.; Soderquist, C. Z.; Smith, F. N.; Mausolf, E. J.; Scheele, R. D. Separation of metallic residues from the dissolution of a high-burnup BWR fuel using nitrogen trifluoride. *Journal of Fluorine Chemistry* **2014,** *162*, 1-8, DOI: 10.1016/j.jfluchem.2014.02.010.
(18) Massoni, N. Study of a nickel-copper filter for the future conditioning of insoluble residues. *Journal of Nuclear Materials* **2016,** *479*, 365-373, DOI: 10.1016/j.jnucmat.2016.07.031.
(19) Alonso, J. I. G.; Thobyschultzendorff, D.; Giovanonne, B.; Glatz, J. P.; Pagliosa, G.; Koch, L. Characterization of spent nuclear-fuel dissolver solutions and dissolution residues by inductively coupled plasma mass-spectrometry. *Journal of Analytical Atomic Spectrometry* **1994,** *9* (11), 1209-1215, DOI: 10.1039/ja9940901209.

(20) Soderquist, C.; Hanson, B. Dissolution of spent nuclear fuel in carbonate–peroxide solution. *Journal of Nuclear Materials* **2010,** *396* (2), 159-162, DOI: https://doi.org/10.1016/j.jnucmat.2009.11.001.
(21) Aihara, H.; Arai, Y.; Shibata, A.; Nomura, K.; Takeuchi, M. Characterization of the Insoluble Sludge from the Dissolution of Irradiated Fast Breeder Reactor Fuel. *Procedia Chemistry* **2016,** *21*, 279-284, DOI: https://doi.org/10.1016/j.proche.2016.10.039.
(22) Myasoedov, B. F.; Kulyako, Y. M. New approaches to reprocessing of oxide nuclear fuel. *Journal of Radioanalytical and Nuclear Chemistry* **2013,** *296* (2), 1127-1131, DOI: 10.1007/s10967-012-2260-6.
(23) Ikeda, Y.; Yasuike, Y.; Takashima, Y.; Park, Y. Y.; Asano, Y.; Tomiyasu, H. O-17 NMR-study on dissolution reaction of UO_2 in nitric-acid - mechanism of electron-transfer. *Journal of Nuclear Science and Technology* **1993,** *30* (9), 962-964, DOI: 10.3327/jnst.30.962.
(24) Glatz, J. P.; Bokelund, H.; Zierfuss, S. Analysis of the off-gas from dissolution of nuclear oxide fuels and carbide fuels in nitric-acid. *Radiochimica Acta* **1990,** *51* (1), 17-22.
(25) Virot, M.; Szenknect, S.; Chave, T.; Dacheux, N.; Moisy, P.; Nikitenko, S. I. Uranium carbide dissolution in nitric solution: Sonication vs. Silent conditions. *Journal of Nuclear Materials* **2013,** *441* (1-3), 421-430, DOI: 10.1016/j.jnucmat.2013.06.021.
(26) Hermann, B. Dissolution of unirradiated UO_2-pellets in nitric acid. *KIT, Technical document* **1984,** *KFK- 3673*, 197.
(27) Cordara, T.; Szenknect, S.; Claparede, L.; Podor, R.; Mesbah, A.; Lavalette, C.; Dacheux, N. Kinetics of dissolution of UO_2 in nitric acid solutions: A multiparametric study of the non-catalysed reaction. *Journal of Nuclear Materials* **2017,** *496* (Supplement C), 251-264, DOI: https://doi.org/10.1016/j.jnucmat.2017.09.038.
(28) Nishimura, K.; Chikazawa, T.; Hasegawa, S.; Tanaka, H.; Ikeda, Y.; Yasuike, Y.; Takashima, Y. Effect of nitrous-acid on dissolution of UO_2 powders in nitric-acid optimal conditions for dissolving UO_2. *Journal of Nuclear Science and Technology* **1995,** *32* (2), 157-159, DOI: 10.3327/jnst.32.157.
(29) Shabbir, M.; Robins, R. G. Kinetics of dissolution of uranium dioxide in nitric acid. *Journal of Applied Chemistry* **1968,** *18*, 129.
(30) Taylor, R. F.; Sharratt, E. W.; De Chazal, L. E. M.; Logsdail, D. H. Dissolution rates of uranium dioxide sintered pellets in nitric acid systems. *Journal of Applied Chemistry* **1963,** *13* (1), 32-40, DOI: 10.1002/jctb.5010130106.
(31) Desigan, N.; Augustine, E.; Murali, R.; Pandey, N. K.; Mudali, U. K.; Natarajan, R.; Joshi, J. B. Dissolution kinetics of Indian PHWR natural UO_2 fuel pellets in nitric acid - Effect of initial acidity and temperature. *Progress in Nuclear Energy* **2015,** *83*, 52-58, DOI: 10.1016/j.pnucene.2015.03.001.
(32) Desigan, N.; Bhatt, N. P.; Pandey, N. K.; Mudali, U. K.; Natarajan, R.; Joshi, J. B. Mechanism of dissolution of nuclear fuel in nitric acid relevant to nuclear fuel reprocessing. *Journal of Radioanalytical and Nuclear Chemistry* **2017,** *312* (1), 141-149, DOI: 10.1007/s10967-017-5208-z.
(33) Ikeda, Y.; Yasuike, Y.; Nishimura, K.; Hasegawa, S.; Mason, C.; Bush, R.; Takashima, Y. Dissolution Behavior of Pulverized Irradiated Fuels in Nitric Acid Solutions. *Journal of Nuclear Science and Technology* **1999,** *36* (4), 358-363, DOI: 10.1080/18811248.1999.9726218.
(34) Vanýsek, P. *CRC Handbook of Chemistry and Physics*, 91st Edition ed.; CRC Press, Bocca Raton, FL.: 2010; p 2610.
(35) Kim, E. H.; Hwang, D. S.; Choung, W. M.; Park, J. H.; Yoo, J. H.; Choi, C. S. Dissolution of UO_2 by photochemical reaction. *Radiochimica Acta* **1998,** *83* (3), 147-151.
(36) Matsui, T.; Ohkawa, M.; Sasaki, R.; Naito, K. Dissolution of the simulated fission-produced Mo-Ru-Rh-Pd alloys in boiling nitric acid solution. *Journal of Nuclear Materials* **1993,** *200* (1), 11-15, DOI: https://doi.org/10.1016/0022-3115(93)90004-I.
(37) Ikeda, Y.; Yasuike, Y.; Takashima, Y.; Nishimura, K.; Hasegawa, S. Acceleration effect of noble-metals on dissolution rate of UO_2 powders in nitric-acid. *Journal of Nuclear Science and Technology* **1993,** *30* (5), 485-487, DOI: 10.3327/jnst.30.485.
(38) Podor, R.; Le Goff, X.; Cordara, T.; Odorico, M.; Favrichon, J.; Claparede, L.; Szenknect, S.; Dacheux, N. 3D-SEM height maps series to monitor materials corrosion and dissolution. *Materials Characterization* **2019,** *under review*.
(39) Martinez, J.; Clavier, N.; Mesbah, A.; Audubert, F.; Le Goff, X. F.; Vigier, N.; Dacheux, N. An original precipitation route toward the preparation and the sintering of highly reactive uranium cerium

dioxide powders. *Journal of Nuclear Materials* **2015,** *462*, 173-181, DOI: 10.1016/j.jnucmat.2015.03.053.
(40) Finger, L. W.; Cox, D. E.; Jephcoat, A. P. A correction for powder diffraction peak asymmetry due to axial divergence. *Journal of Applied Crystallography* **1994,** *27*, 892-900, DOI: 10.1107/s0021889894004218.
(41) Roisnel, T.; Rodriguez-Carvajal, J. *WinPLOTR: A Windows tool for powder diffraction pattern analysis*, 2001; Vol. 378, p 118-123.
(42) Dalger, T.; Szenknect, S.; Tocino, F.; Claparede, L.; Mesbah, A.; Moisy, P.; Dacheux, N. Kinetics of dissolution of $Th_{0.25}U_{0.75}O_2$ sintered pellets in various acidic conditions. *Journal of Nuclear Materials* **2018,** *510*, 109-122, DOI: https://doi.org/10.1016/j.jnucmat.2018.07.050.
(43) Schindelin, J.; Arganda-Carreras, I.; Frise, E.; Kaynig, V.; Longair, M.; Pietzsch, T.; Preibisch, S.; Rueden, C.; Saalfeld, S.; Schmid, B.; Tinevez, J.-Y.; White, D. J.; Hartenstein, V.; Eliceiri, K.; Tomancak, P.; Cardona, A. Fiji: an open-source platform for biological-image analysis. *Nature Methods* **2012,** *9*, 676, DOI: 10.1038/nmeth.2019

https://www.nature.com/articles/nmeth.2019#supplementary-information.
(44) Lowe, D. G. Distinctive Image Features from Scale-Invariant Keypoints. *International Journal of Computer Vision* **2004,** *60* (2), 91-110, DOI: 10.1023/b:visi.0000029664.99615.94.
(45) Thevenaz, P. StackReg: An ImageJ plugin for the recursive alignment of a stack of images.
(46) Franco, L. A.; Sinatora, A. 3D surface parameters (ISO 25178-2): Actual meaning of Spk and its relationship to Vmp. *Precision Engineering* **2015,** *40*, 106-111, DOI: https://doi.org/10.1016/j.precisioneng.2014.10.011.
(47) Desgranges, L.; Baldinozzi, G. Oxygen Lattice Distortions and U Oxidation States in UO_{2+x} Fluorite Structures. In *Scientific Basis for Nuclear Waste Management Xxxii*; Hyatt, N. C.; Pickett, D. A.; Rebak, R. B., Eds.; 2009; p 225.
(48) Vaudano, A. Quelques caractéristiques des combustibles nucléaires, intéressant leur traitement. In *Monographie DEN. Le traitement-recyclage du combustible nucléaire usé.*; CEA Saclay et Le Moniteur: 2008; pp 37-41.
(49) Ikeda, Y.; Yasuike, Y.; Nishimura, K.; Hasegawa, S.; Takashima, Y. Kinetic-study on dissolution of UO_2 powders in nitric-acid. *Journal of Nuclear Materials* **1995,** *224* (3), 266-272, DOI: 10.1016/0022-3115(95)00059-3.
(50) Fukasawa, T.; Ozawa, Y. Relationship between dissolution rate of uranium dioxide pellets in nitric acid solutions and their porosity. *Journal of Radioanalytical and Nuclear Chemistry* **1986,** *106* (6), 345-356, DOI: 10.1007/bf02163667.
(51) Corkhill, C. L.; Myllykyla, E.; Bailey, D. J.; Thornber, S. M.; Qi, J.; Maldonado, P.; Stennett, M. C.; Hamilton, A.; Hyatt, N. C. Contribution of Energetically Reactive Surface Features to the Dissolution of CeO_2 and ThO_2 Analogues for Spent Nuclear Fuel Microstructures. *Acs Applied Materials & Interfaces* **2014,** *6* (15), 12279-12289, DOI: 10.1021/am5018978.
(52) Horlait, D.; Claparede, L.; Tocino, F.; Clavier, N.; Ravaux, J.; Szenknect, S.; Podor, R.; Dacheux, N. Environmental SEM monitoring of $Ce_{1-x}Ln_xO_{2-x/2}$ mixed-oxide microstructural evolution during dissolution. *Journal of Materials Chemistry A* **2014,** *2* (15), 5193-5203, DOI: 10.1039/c3ta14623e.
(53) Corkhill, C. L.; Bailey, D. J.; Tocino, F. Y.; Stennett, M. C.; Miller, J. A.; Provis, J. L.; Travis, K. P.; Hyatt, N. C. Role of Microstructure and Surface Defects on the Dissolution Kinetics of CeO_2, a UO_2 Fuel Analogue. *Acs Applied Materials & Interfaces* **2016,** *8* (16), 10562-10571, DOI: 10.1021/acsami.5b11323.
(54) Szenknect, S.; Finkeldei, S.; Brandt, F.; Ravaux, J.; Odorico, M.; Podor, R.; Lautru, J.; Dacheux, N.; Bosbach, D. Monitoring the microstructural evolution of $Nd_2Zr_2O_7$ pyrochlore during dissolution at 90 °C in 4 M HCl: Implications regarding the evaluation of the chemical durability. *Journal of Nuclear Materials* **2017,** *496* (Supplement C), 97-108, DOI: https://doi.org/10.1016/j.jnucmat.2017.09.029.
(55) Fischer, C.; Finkeldei, S.; Brandt, F.; Bosbach, D.; Luttge, A. Direct Measurement of Surface Dissolution Rates in Potential Nuclear Waste Forms: The Example of Pyrochlore. *Acs Applied Materials & Interfaces* **2015,** *7* (32), 17857-17865, DOI: 10.1021/acsami.5b04281.

(56) Hojo, H.; Mizoguchi, T.; Ohta, H.; Findlay, S. D.; Shibata, N.; Yamamoto, T.; Ikuhara, Y. Atomic Structure of a CeO2 Grain Boundary: The Role of Oxygen Vacancies. *Nano Letters* **2010,** *10* (11), 4668-4672, DOI: 10.1021/nl1029336.
(57) Matsui, K.; Yoshida, H.; Ikuhara, Y. Grain-boundary structure and microstructure development mechanism in 2–8 mol% yttria-stabilized zirconia polycrystals. *Acta Materialia* **2008,** *56* (6), 1315-1325, DOI: http://dx.doi.org/10.1016/j.actamat.2007.11.026.
(58) Lei, Y. Y.; Ito, Y.; Browning, N. D.; Mazanec, T. J. Segregation effects at grain boundaries in fluorite-structured ceramics. *J Am Ceram Soc* **2002,** *85* (9), 2359-2363, DOI: 10.1111/j.1151-2916.2002.tb00460.x.
(59) Zhao, Y. F.; Chen, J. Comparative studies on the dissolution of ceramic UO2 pellets in nitric acid by microwave and conventional heating. *Radiochimica Acta* **2008,** *96* (8), 467-471, DOI: 10.1524/ract.2008.1507.
(60) Uriarte, A. L.; Rainey, R. H. *Dissolution of high-density UO_2, PuO_2 and UO_2-PuO_2 pellets in inorganic acids.*; Oak Ridge National Laboratory: 1965; p 81.
(61) Shabbir, M.; Robins, R. G. Effect of crystallographic orientation on dissolution of uranium dioxide in nitric acid. *Journal of Nuclear Materials* **1968,** *25* (2), 236-237, DOI: 10.1016/0022-3115(68)90049-4.
(62) Marc, P.; Magnaldo, A.; Vaudano, A.; Delahaye, T.; Schaer, É. Dissolution of uranium dioxide in nitric acid media: what do we know? *EPJ Nuclear Sci. Technol.* **2017,** *3*, 13.

For Table of Contents only:

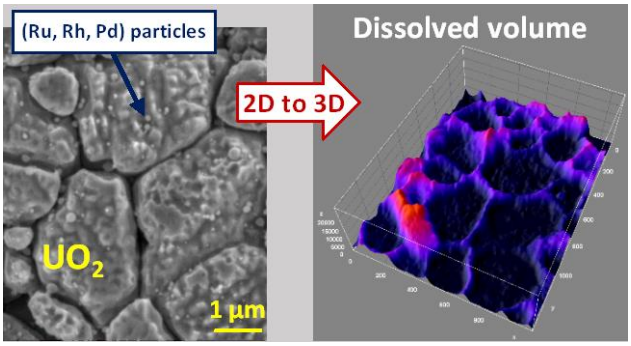

- Uranium dioxide dense pellet containing 3 mol.% platinum group metals (PGMs) was synthesized
- The characterization techniques performed revealed a microstructure similar to that of spent nuclear fuel
- Dissolution tests were performed in nitric acid medium and demonstrated that in the presence of PGMs, the uranium dissolution rate was increased
- The evolution of the solid/liquid interface during dissolution was monitored by means of 3D reconstructions of stereoscopic ESEM micrographs
- Preferential dissolution zones in the vicinity of the PGM particles were observed and microscopic dissolution rates were determined for several regions of interest